J Appl Electrochem (2011) 41:355–361
DOI 10.1007/s10800-010-0239-y

SHORT COMMUNICATION

Mapping of pH gradients in a micrometric occluded cell: comparison with a pseudo-2D transport model

Aurélien Percheron · Bruno Vuillemin · Roland Oltra · Laurent Markey

Received: 2 February 2010 / Accepted: 24 October 2010 / Published online: 5 November 2010

Abstract This paper presents an experiment suitable for validating calculated pH gradients inside an occluded cell. Photolithography is used to pattern a 10 μm thick cavity former on a stainless steel surface, providing a rigorously controlled experimental support for transport models such as those proposed in the fields of crevice corrosion or cathodic delamination. pH gradients over the electrode are measured by total internal reflection fluorescence microscopy (TIRFM) during cathodic polarization under potentiostatic and galvanostatic conditions. The pH profiles calculated using a pseudo-two-dimensional (pseudo-2D) transport model agree well with experimental data, except that the rates of pH increase observed experimentally are much slower than the simulated ones.

Keywords pH distribution · Crevice · FEM modelling · TIRFM

1 Introduction

The outputs of mathematical models developed recently in the field of corrosion in confined volumes, either during a cathodic delamination process [1, 2] or in the field of crevice corrosion [3], are often given in terms of pH distributions along the cavity. Unfortunately, few experimental results allow checking of the validity of these models, and it is noteworthy that recent papers dealing with modelling of crevice corrosion still rest on a pioneering paper including experimental pH profile measurements [4]. This raises the question of the reliability of in situ experimental results used to develop predictive models. Some studies have reported pH distributions over large-scale (about 1 mm thick) crevices polarized cathodically, using conventional microelectrodes [5]. However, unlike optical methods [6, 7], such techniques are difficult to develop for cavity thicknesses that are more representative of practical systems, i.e., in the micrometre range. To do this, Dunn et al. fitted pH electrodes to a crevice former pressed against the metal surface, the electrolyte thickness being controlled by the roughness of the metal. However, their results under anodic polarization were difficult to interpret, most probably because of initiation of localized corrosion in the crevice [8]. In a previous study, we developed total internal reflection fluorescence microscopy (TIRFM) [6] to measure the pH distribution over micrometre-thick cavities, the objective being to observe the minimum pH predicted in numerical simulations of crevice corrosion processes [9]. Unlike potentiometric methods, this technique allows a 2D mapping of the pH, and is not sensitive to electric fields that can be encountered through externally polarized occluded cells. In this study (as in [8]), the crevice gap was not rigorously controlled because it depended on the roughness of the metal pressed against the pH sensor.

The objective of the present study was to determine experimental pH profiles over an electrode polarized cathodically in a cavity with a well-controlled geometry to fit, as well as possible, to ideal cavities considered in modelling studies. To do this we developed an original procedure to pattern these cavities by photolithography, as proposed in [10]. Then, we checked to what extent the pH profiles measured experimentally could be simulated using a pseudo-2D mass transport model. The advantages of cathodic versus anodic polarization are: (i) a low modification of the chemical composition of the occluded cell

A. Percheron · B. Vuillemin (✉) · R. Oltra · L. Markey
LICB UMR 5209 CNRS Université de Bourgogne,
BP 47 870, 21078 Dijon, France
e-mail: bruno.vuillemin@u-bourgogne.fr

(unlike in crevice corrosion situations), (ii) a better dynamic response of the optical sensor obtained in the alkaline domain [6].

2 Experimental conditions

Cylindrical 304 stainless steel samples (ARCELOR Mittal) were used (diameter = 11 mm, height = 9 mm). To avoid any electrochemical reaction on the walls of the cylinder, the samples were coated with a cataphoretic paint. A stainless steel ring machined in the same metal was accurately adjusted to the sample. The role of this ring was: (i) to hold the sample during polishing, thus allowing maintenance of a perfect right angle between the wall of the cylinder and its upper (disc) surface, (ii) to prevent any accumulation of resin during spin coating (see further). The sample (with the ring) was then mechanically polished with SiC paper and several grades of diamond paste down to 1 μm, followed by ultrasonic cleaning in ethanol. It was then dried under a nitrogen flux and stored for 12 h at 110 °C. As shown in Fig. 1, a 2 × 2.5 mm rectangular cavity was patterned on the top surface of the cylinder using photolithography with an SU-8 2000 negative epoxy-type photoresist (MicroChem®). A spin-coating technique was used to obtain a uniform thickness of the resin. For this purpose, the sample and its ring were mounted on the stage of a spin coater (SPINCOATER® P6700), and the top surface of the sample was completely covered with the resin. Then, the spin-coating sequence sketched in Fig. 1 was performed. The rotation speed during the last step allowed control of the thickness (after curing) of the coating, as shown in Fig. 1. Then, the sample with its surrounding ring was laid on a hotplate (Präzitherm®) at 65 °C for 20 min. During this 'soft bake', the solvent was partially removed from the resin, leading to a more viscous layer. Before a second curing (15 min at 95 °C), the ring was separated from the sample to obtain a uniform thickness along the rim of the sample surface. In the absence of a surrounding ring, an accumulation of resin was observed after the spin coating, leading to a greater thickness on the rim of the sample. With the method presented here, this 'defect' was swept along towards the ring. UV cross-linking was performed by irradiating the surface through a mask with a Karl Suss UV MJB21® Mask Aligner. For a final thickness of about 10 μm, the fluence of the radiation was approximately 400 mJ cm^{-2}. A post-bake was then performed consisting of heating the sample on the hotplate for 10 min at 65 °C, and 15 min at 95 °C. Then, the area not irradiated (cavity) was dissolved by immersing the sample in an SU-8 developer bath (MicroChem®) under stirring conditions for 6 min. The surface was then rinsed with isopropanol and dried under a nitrogen flux. Control of the quality of the coating (thickness, homogeneity) was checked with a stylus profilometer (Veeco Dektak® 6 M—vertical resolution 0.5 nm). For the present study, profiles performed over a distance of 3 mm indicate a thickness of 10 ± 0.1 μm.

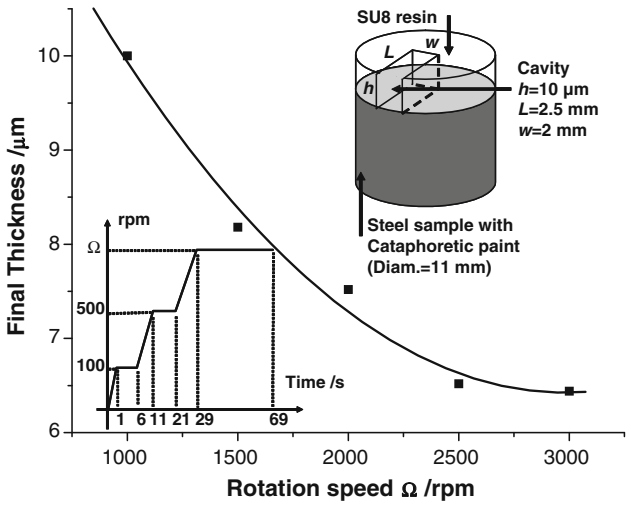

Fig. 1 Thickness of the resin after curing versus rotation speed, Ω, during the last step of the spin-coating sequence (*inset*: spin-coating sequence and scheme of the electrode and cavity)

The pH distribution in the cavity during sample polarization was measured by using a TIRFM technique developed especially for this purpose [6] and sketched in Fig. 2. This technique is based on excitation with a blue laser (Cobolt®, $\lambda = 488$ nm) of fluorescein trapped in a 300 nm thick silica polymer film deposited by a sol–gel method on a glass slide. A detailed description of the coating process was given elsewhere [6]. The main advantage of the encapsulation of the fluorescent dye for electrochemical applications (in comparison with classical TIRFM techniques where the dye is in solution) is the impossibility for the dye to influence the electrochemical reactions occurring on the electrode surface. Thanks to a prism glued on the top side of the sensor with a matching index liquid, and due to the very closed values of the optical indexes of the glass slide ($n_1 = 1.45$) and of the sensing layer ($n_2 = 1.40$) it is possible to inject the laser beam with an angle allowing internal reflexions in the glass slide that behaves like a waveguide. These total internal reflection conditions create an evanescent wave that interacts with the fluorescein entrapped in the silica matrix. The resulting fluorescence signal emitted by the fluorescein at $\lambda = 514$ nm is collected and filtered using a conventional microscope equipped with a CCD camera (Hamamatsu® C8484-05G) located above the sensor. The fluorescence intensity is measured and normalized versus the maximum intensity obtained in alkaline (pH >10) conditions. As can be seen in Fig. 3a, the calibration curve demonstrates a sigmoidal dependence of this fluorescence ratio as a function of the

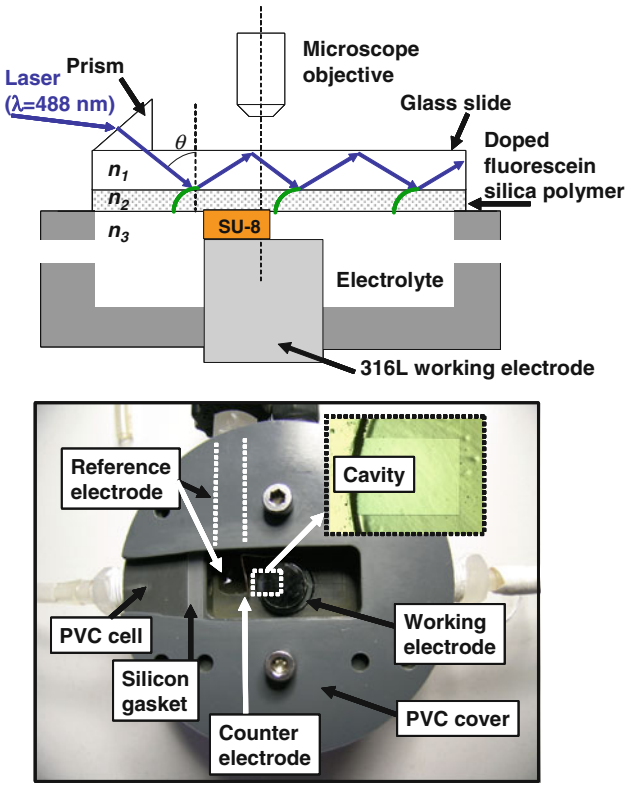

Fig. 2 Schematic side view of the electrochemical cell with the TIRFM technique (*top*). Top-view photograph of the electrochemical cell (*bottom*). The sensor (not shown) is pressed against the working electrode surface using the PVC cover

pH of the solution, in a pH range between 3 and 10. The time response of the sensor was estimated by successively injecting two solutions of pH 5.0 and 7.9, respectively, in a flow cell configuration. Figure 3b indicates that this time response is around 15 s.

For pH measurements in occluded cells, the sample was pressed on the pH sensor in a 1 M NaCl solution (pH 5), and the resulting cavity was cathodically polarized versus a saturated calomel electrode (SCE). This method is very well adapted to the measurement of pH distribution in cavities with such an aspect ratio (length ≫ thickness), because pH gradients are expected only in the horizontal direction. In other words, the pH measured at a distance of 10 μm from the surface is identical to the pH on the sample surface.

3 Mass transport model

Experimental pH distributions were compared with calculated profiles obtained by the finite element method (FEM) using commercial software (COMSOL® Multiphysics). The geometry and mesh conditions of the system are given in Fig. 4. As will be seen in the experimental results, it was necessary to consider the external medium because pH modifications were also observed at a distance of about 100 μm from the cavity mouth. Considering the previous remark about the aspect ratio of the electrochemical cell, the chemical gradients normal to the metal surface were neglected. This is the reason that we developed a pseudo-2D model for the occluded cell (the cavity being assumed infinite in the width direction), accounting only for its length, L, and its thickness, h, with h = mesh size in the cavity. The Nernst–Planck equation was solved over the total domain

$$D_i[\nabla^2 C_i + \frac{z_i F}{RT}\nabla(C_i \nabla\Phi)] + R_i = \frac{\partial C_i}{\partial t}$$

The meanings of the symbols and values of the parameters are reported in Table 1. Five aqueous species were considered: Cl^-, Na^+, H^+, OH^- and O_2. Electroneutrality

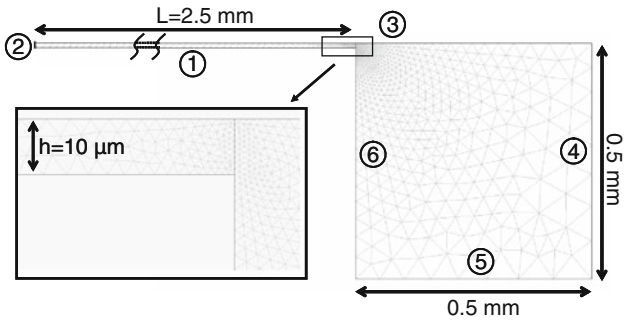

Fig. 4 Geometry and mesh conditions used for the model

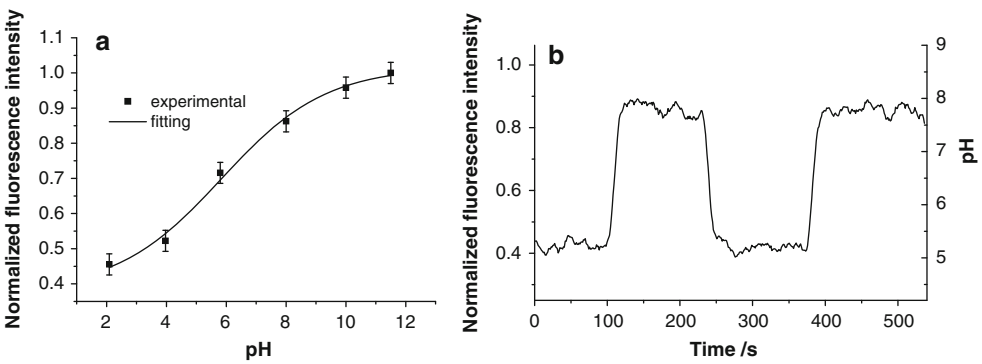

Fig. 3 **a** Calibration curve for a fluorescein doped silica layer. The fluorescence intensity is normalized versus the maximum intensity obtained at pH 11.5. **b** Time response of the optical pH sensor during successive injections of pH 5.0 and 7.9 solutions

Table 1 Symbol descriptions and parameter values used for the simulations

$b_{O_2} b_{O2}$	Tafel coefficient for O_2 reduction	50 mV [12]
b_H	Tafel coefficient for H^+ reduction	50 mV [13]
C_i	Concentration of species i	mol m^{-3}
D_{Cl}, D_{Na}	Diffusion coefficients for Cl^- and Na^+	10^{-9} m^2 s^{-1}
D_H	Diffusion coefficient for H^+	9.3×10^{-9} m^2 s^{-1}
D_{OH}	Diffusion coefficient for OH^-	5.3×10^{-9} m^2 s^{-1}
D_{O_2}	Diffusion coefficient for O_2	2.4×10^{-9} m^2 s^{-1}
$E_{O_2}^{Eq}$	Nernst equilibrium potential for O_2/H_2O	0.455 V/SCE [12]
F	Faraday's constant	96487 C mol^{-1}
h	Thickness of the cavity	10 μm
i_{O_2}	Current density for O_2 reduction	A m^{-2} [12]
$i_{O_2}^0$	Exchange current density for O_2 reduction	3.22×10^{-9} A m mol^{-1} [12]
i_H	Current density for H^+ reduction	A m^{-2} [13]
i_H^0	Exchange current density for H^+ reduction	2×10^{-7} A m mol^{-1} [13]
k_{wb}	Backward reaction rate constant for H_2O autoprotolysis	10^{11} m^3 mol^{-1} s^{-1}
k_{wf}	Forward reaction rate constant for H_2O autoprotolysis	10^3 mol m^{-3} s^{-1}
K_w	Equilibrium constant for water autoprotolysis	10^{-14}
V_m	Potential of the metal	V/SCE
R_i	Source term for species i	mol m^{-3} s^{-1}
Φ	Potential in solution	V

was assumed in the electrolyte. Water autoprotolysis was the only chemical reaction considered (imposed at equilibrium). Then the source terms R_i for each species were expressed as

$$R_{Cl^-} = R_{Na^+} = 0$$
$$R_{O_2} = 0$$
$$R_{H^+} = k_{wf} - k_{wb} \cdot C_{H^+} \cdot C_{OH^-}$$
$$R_{OH^-} = k_{wf} - k_{wb} \cdot C_{H^+} \cdot C_{OH^-}$$

where k_{wf} and k_{wb}, the forward and backward reaction rate constants for autoprotolysis of water, respectively, are kept sufficiently high to maintain the equilibrium condition for this reaction. Both oxygen and proton reduction were assumed to occur at the metal surface (boundary 1). Considering the experimental difficulty in determining (and then finding) reliable kinetics parameters for oxygen reduction on non-noble metals, we used the data reported by Jovancicevic and Bockris on steel at pH 9 [11, 12]. In our study, we used exactly the same parameters, leading to the following expression for the cathodic current for oxygen reduction:

$$i_{O_2} = -i_{O_2}^0 \cdot C_{O_2} \cdot \exp\left[\frac{\left(V_m - \Phi - E_{O_2}^{Eq}\right)}{b_{O_2}}\right]$$

with $E_{O_2}^{Eq}$ the Nernst equilibrium potential for the O_2/H_2O redox couple at pH 9 and for an O_2 reference concentration of 1.24 mol m^{-3} ($E_{O_2}^{Eq} = 0.455V/SCE$). Similarly, the cathodic contribution for proton reduction was expressed as [13]

$$i_H = -i_H^0 \cdot C_H \cdot \exp\left[\frac{(V_m - \Phi)}{b_H}\right]$$

The pH distribution was also calculated under galvanostatic conditions. In these conditions, a constant current density i_{red} was imposed over the whole of the electrode surface.

At boundaries 4 and 5, bulk conditions (identical to initial conditions) were imposed with: $[Na^+] = [Cl^-] = 1000$ mol m^{-3}, $[H^+] = 10^{-2}$ mol m^{-3} (pH 5), $[OH^-] = 10^{-6}$ mol m^{-3}, $[O_2] = 0.26$ mol m^{-3} and $\Phi = 0$ V. The other boundaries were considered as insulators.

4 Results and discussion

Experimental pH profiles obtained in galvanostatic ($I = -0.05$ μA) and potentiostatic ($E = -0.8$ V/SCE) conditions are given in Fig. 5. It must be emphasized that special attention has been paid to the repeatability of these results (confidence interval: ±1 pH unit), and to the reliability of the optical method used for the pH measurements. Moreover, as can be seen in Fig. 3b, the time response of the pH sensor (approximately 15 s in these conditions) is very small in comparison with the time evolution of the pH profiles. Moreover, photobleaching of the pH-sensing layer, leading to a decrease of the efficiency of the sensor, has been limited by reducing the number of pH measurements. This photobleaching effect is most probably the reason why a slight pH decrease is observed at $t > 20$ min

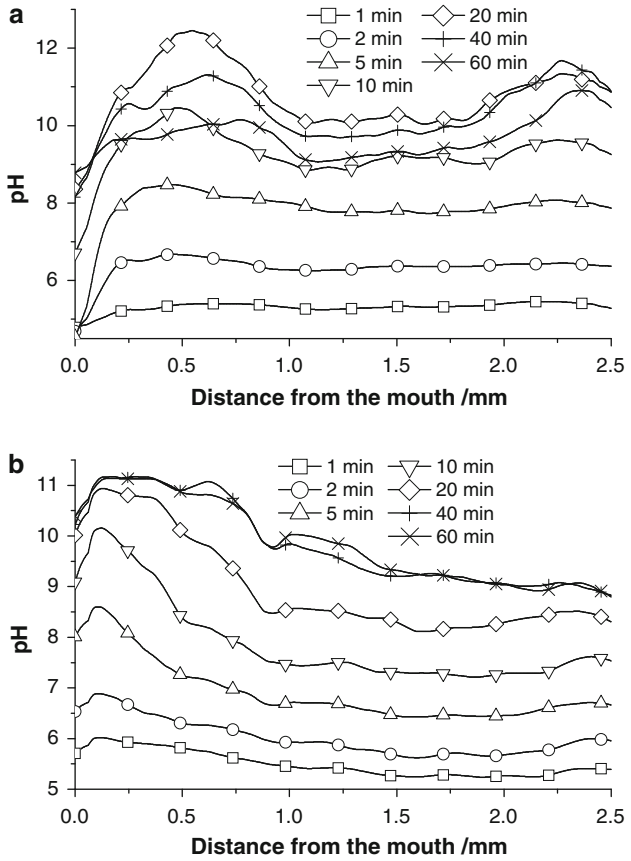

Fig. 5 Experimental pH profiles vs time under: **a** galvanostatic conditions ($I = -0.05$ μA), **b** potentiostatic conditions ($E = -0.8$ V/SCE). Bulk solution: NaCl 1 M, pH 5

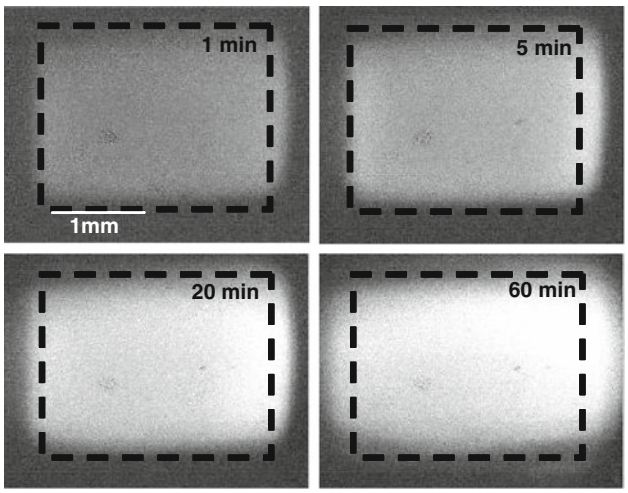

Fig. 6 Sequence of fluorescence ratio images obtained under potentiostatic conditions ($E = -0.8$ V/SCE). The *dashed lines* represent the limit of the cavity, with the mouth (bulk electrolyte) on the right

in Fig. 5a. It can be seen that the natural convection of the external bulk medium is never sufficient to maintain the initial pH (i.e., pH 5) at the mouth of the occluded electrode. Figure 6 presents a sequence of fluorescence ratio images obtained under potentiostatic conditions. This sequence clearly indicates that the hydroxyl ions produced in the cavity during cathodic polarization are mainly transported in the bulk medium through the cavity mouth, and that their transport towards the cavity edges seems to be negligible (i.e., there is weak alkalinization of the SU-8 resin/sensor interface). Figure 7 shows the potential and current transients obtained under galvanostatic and potentiostatic conditions, respectively. In both conditions, a comparison with pH transients shown in Fig. 5 indicates that steady current and potential are more rapidly achieved, especially in potentiostatic conditions, than the pH steady state.

It must be emphasized that giving a physical meaning to these potential and current transients is not as easy as in bulk conditions, considering the geometry of the occluded electrochemical cell, and the resulting non-homogeneity of the potential and current distributions on the working electrode. A simple application of Faraday's law (with $[O_2] = 0.26$ mol m^{-3}, $i_{red} = 0.01$ A m^{-2}, electrode surface area $= 5 \times 10^{-6}$ m^{-2}, volume of cavity $= 5 \times 10^{-11}$ m^{-3}) indicates that total deoxygenation of the cavity would occur in 100 s. At this time, neglecting exchange with the bulk medium, and the water and the passive film reduction, the value expected for the average pH in the cavity would be 10. As indicated in Fig. 8a, the FEM simulation is in good agreement with this rough calculation. The simulation indicates that a steady oxygen gradient is obtained in about 100 s, with $[O_2] < 2 \times 10^{-6}$ mol L^{-1} for distances greater than 0.5 mm from the cavity mouth. Moreover, in galvanostatic conditions, we systematically measured a higher pH on the edges of the electrode for $t > 5$ min. This effect, originating most probably from a non-uniform current distribution over the electrode, is not visible in the simulated pH profiles, because a uniform reduction flux is imposed as a boundary condition. This could be the reason that the simulated rate of alkalinization is one to two orders of magnitude higher than that measured experimentally.

Under potentiostatic conditions, it can be observed that higher pH values are measured in the vicinity of the mouth (Fig. 5b). This observation is in agreement with experimental results reported by Perdomo and Song with much larger cavities [5]. It can be explained by an increase in the ohmic drop along the crevice (measured in [5]), and a higher oxygen concentration in the vicinity of the mouth. Calculated pH profiles shown in Fig. 8b are similar to those obtained experimentally, but the rate of pH increase is once again higher (by more than three orders of magnitude) than that obtained experimentally. This discrepancy between the experimental and simulated rates of alkalinization of the cavity is not surprising, because under potentiostatic

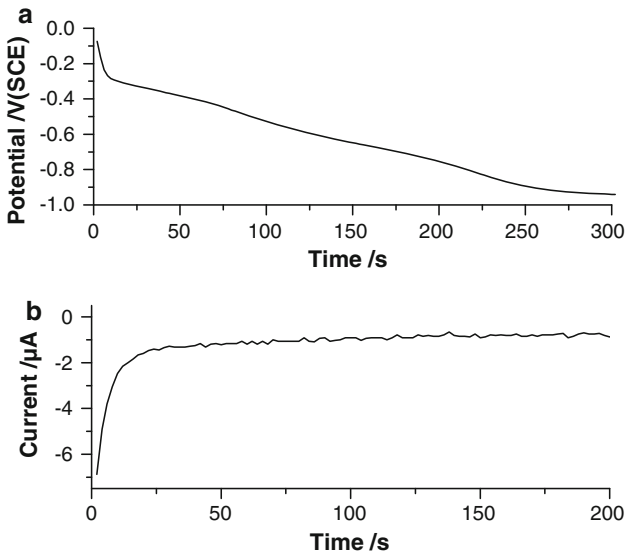

Fig. 7 Potential and current transients obtained respectively under: **a** galvanostatic ($I = -0.05$ μA), **b** potentiostatic ($E = -0.8$ V/SCE) conditions. Bulk solution: NaCl 1 M, pH 5

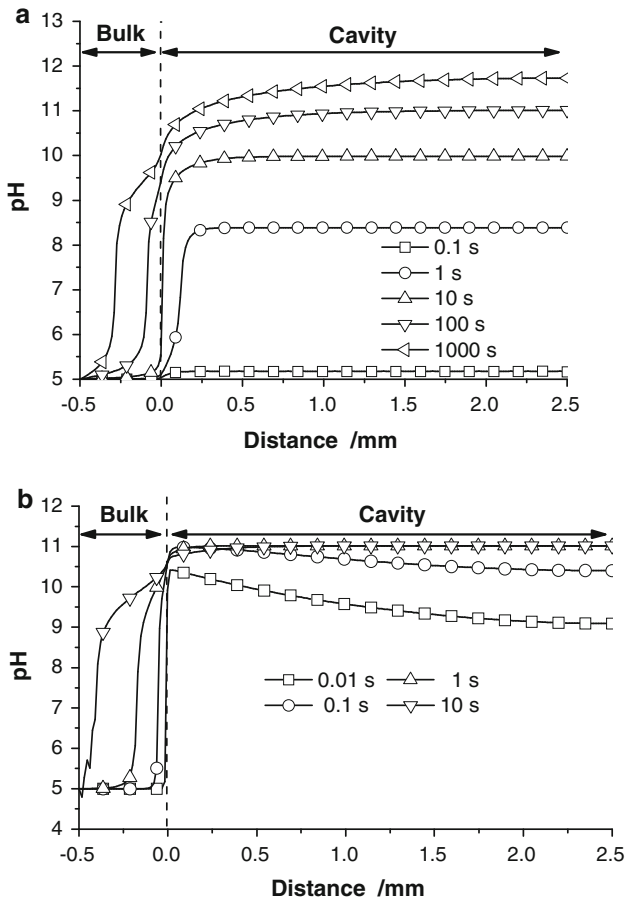

Fig. 8 Time evolution of pH profiles calculated under: **a** galvanostatic ($I = -0.05$ μA), **b** potentiostatic ($E = -0.8$ V/SCE) conditions

conditions the calculated current transient accounts only for faradaic processes, capacitive effects being ignored. Moreover, the electrolyte resistance calculated in a pseudo-2D simulation, and consequently the resulting ohmic drop in the cavity, is most probably higher. In this case, using a 2D geometry implies effectively an infinite cavity in the width direction, leading to an underestimation of the electrolyte resistance. In a previous study, we showed that this electrolyte resistance in an occluded area could be simulated, in the absence of concentration gradients, only by considering the actual 3D geometry [14].

5 Conclusion

An original photolithography technique for designing micrometre-thick cavities with rigorously controlled dimensions was developed, and it was demonstrated that it is possible to measure accurately the pH distribution over such cavities patterned on stainless steel substrates polarized cathodically. The pH profiles calculated under potentiostatic and galvanostatic conditions using a pseudo-2D transport model present a similar trend to those obtained experimentally, but are not completely satisfactory. Some improvements in the model, but also in the experimental procedure, must be achieved to have a better correlation between the experimental and calculated pH profiles. It appears that the experimental approach must be carried out using a low-current potentiostat, to lower the polarization, and thus the resulting rate of alkalinization. In such conditions, capacitive and resistive effects could be limited. It appears that such discrepancies must be addressed before simulating pH evolution under anodic conditions, as encountered in crevice corrosion situations, where a much more complex chemistry develops in the confined zone.

References

1. Huang MW, Allely C, Ogle K, Orazem ME (2008) J Electrochem Soc 155:279
2. Song FM, Kirk DW, Graydon JW, Cormack DE (2002) Corrosion 58:1015
3. Vankeerberghen M, Weyns G, Gavrilov S, Henshaw J, Deconinck J (2009) J Nucl Mater 385:517
4. Alavi A, Cottis RA (1987) Corros Sci 27:443
5. Perdomo JJ, Song I (2000) Corros Sci 42:1389
6. Loete F, Vuillemin B, Oltra R et al (2006) Electrochem Commun 8:1016
7. Hotta H, Tatsuno K, Hattori Y, Hashimoto T, Uehara M, Tsunoda K (2008) Electrochem Commun 10:1351
8. Shridar N, Dunn DS (1994) Corrosion 50:857
9. Vuillemin B, Oltra R, Cottis RA, Crusset D (2007) Electrochim Acta 52:7570
10. Lee JS, Reed ML, Kelly RG (2004) J Electrochem Soc 151:423

11. Jovancicevic V, Bockris JO'M (1986) J Electrochem Soc 133:1797
12. Song FM (2008) Corros Sci 50:3287
13. Turnbull A, Gardner MK (1982) Corros Sci 22:661
14. Rubin A, Oltra R, Vuillemin B, Ogle K (2008) Electrochim Acta 53:6484